Quaternary Geochronology 47 (2018) 72–80

Contents lists available at ScienceDirect

Quaternary Geochronology

journal homepage: www.elsevier.com/locate/quageo

Asian monsoon dynamics at Dansgaard/Oeschger events 14–8 and Heinrich events 5–4 in northern China

Jinguo Dong[a,*], Chuan-Chou Shen[b,**], Xinggong Kong[c], Yi Wang[d], Fucai Duan[b,e]

[a] College of Geosciences, Nantong University, Nantong, Jiangsu, 226007, China
[b] High-Precision Mass Spectrometry and Environment Change Laboratory (HISPEC), Department of Geosciences, National Taiwan University, Taipei, 106, Taiwan, ROC
[c] College of Geosciences, Nanjing Normal University, Nanjing, Jiangsu, 210097, China
[d] Department of Geography, School of Global Studies, University of Sussex, Brighton, BN1 9QJ, UK
[e] College of Geography and Environmental Sciences, Zhejiang Normal University, Jinhua, Zhejiang, 321004, China

ARTICLE INFO

Keywords:
Northern China
Stalagmite
Asian summer monsoon
Last glacial period
Heinrich events
DO oscillations

ABSTRACT

A precisely ^{230}Th-dated stalagmite oxygen isotope (δ^{18}O) record from Dragon Cave, Shanxi Province, northern China, is proposed to reconstruct the millennial-scale changes of the East Asian Summer monsoon (EASM) during the period 53.2–1.3 ka BP (before 1950 AD). Our record shows significant millennial-scale oscillations that match in timing, characteristic, and duration with the Dansgaard/Oeschger (DO) events 14–8 and the Heinrich events 5, 4, 2, and 1 (hereafter H5, H4, H2 and H1) in high-latitude regions of the Northern Hemisphere. Especially, the H5 event is well constrained from 48.1 to 46.9 ka BP with ten ^{230}Th dates. Our chronology supports the NGRIP GICC05 timescale from 50 to 38 ka BP. A comprehensive comparison of the Chinese speleothem records from different regions along a north-south transect shows a unique trend towards more negative δ^{18}O values from 48.0 to 38.0 ka BP, suggesting that an intensified Asian summer monsoon (ASM) across the whole monsoonal China during the interval. We speculate that the joint effect, from both the cooling of the Southern Hemisphere and the enhanced land-sea temperature contrast due to the rising summer insolation, is capable to regulate the low-latitude large-scale atmospheric circulation patterns and exert significant influences on the long-term ASM variations during the middle of Marine Isotope Stage 3.

1. Introduction

The Dansgaard-Oeschger (DO) cycles, first recognized in Greenland in 1993 (Dansgaard et al., 1993), are characterized by an abrupt initial warming, followed by a gradual cooling (Dansgaard et al., 1993; Meese et al., 1997). These typical millennial-scale abrupt events have been recognized in numerous palaeoclimatic archives worldwide (Porter and An, 1995; Voelker, 2002; Wang et al., 2001; EPICA community Members, 2006; Kanner et al., 2012; Caley et al., 2013; Moseley et al., 2014). However, the key signature of those abrupt events is quite different in their characteristics and timings in different climatic zones (Dansgaard et al., 1993; Genty et al., 2003; EPICA community Members, 2006), such as in the Asian monsoon region (Wang et al., 2001; Burns et al., 2003; Duan et al., 2014) and in the Southern Hemisphere (EPICA community Members, 2006). Various hypotheses were proposed to explain these discrepancies, including the bi-polar seesaw (Broecker, 1998; Blunier and Brook, 2001; Landais et al., 2015), tropical ocean processes (Pierrehumbert, 2000; Stott et al., 2002) and Southern Hemisphere forcing (Rohling et al., 2003, 2009; Cai et al., 2006; Shen et al., 2010; An et al., 2011; Chen et al., 2016).

During the last glacial period, enormous icebergs intermittently calved from the ice shelves and traversed the North Atlantic. These so-called Heinrich (H) events were recorded at least six times through the ice-rafted debris (IRD) preserved in marine sediment (Heinrich, 1988; Hemming, 2004). During the H events, the extensive amounts of fresh water entering the North Atlantic attenuated the density-driven thermohaline circulation and led to climate changes worldwide (Hemming, 2004). The Asian summer monsoon (ASM) intensity was also decreased during the H events through ocean-atmospheric teleconnections (Porter and An, 1995; Wang et al., 2001; Zhao et al., 2010).

In recent years, speleothem-based investigations led to some significant advances in the reconstruction of the past ASM variability mainly with the advantages of absolute U-series chronological techniques (Wang et al., 2001, 2008; Yuan et al., 2004; Cheng et al., 2009, 2016). Hulu Cave δ^{18}O record in eastern China is usually regarded as an important “chronology reference dataset”, which displays significant

* Corresponding author.
** Corresponding author.
E-mail addresses: dongjinguo1111@163.com (J. Dong), river@ntu.edu.tw (C.-C. Shen).

https://doi.org/10.1016/j.quageo.2018.05.012
Received 9 January 2018; Received in revised form 9 May 2018; Accepted 15 May 2018
Available online 17 May 2018
1871-1014/

millennial-scale variations that can be closely matched with the Greenland Interstadials and Stadials. It also provides acceptable age controls on DO 21–1. However, the association of speleothem-derived ASM variations with millennial-scale temperature changes in northern high latitudes is not straightforward during the period from 50 to 38 ka BP (before 1950 AD) (Wang et al., 2001; Burns et al., 2003). It is still difficult, for example, to determine whether the actual timing of the DO 12 is at 48 or 45 ka BP, even many speleothem $\delta^{18}O$ records in the Eurasia continent have been published (Wang et al., 2001; Genty et al., 2003; Spötl et al., 2006; Fleitmann et al., 2009; Zhou et al., 2014; Moseley et al., 2014). A detailed comparison of the absolute-dated Hulu-Sofular records with the NGRIP on the GICC05 timescale (Fleitmann et al., 2009) shows that age differences are remarkably increased from 38 to 49 ka BP, with a maximum difference of 800 years at the onset of DO 12. This age difference becomes almost zero near 55 ka BP (DO 14) (Wang et al., 2001; Svensson et al., 2008; Fleitmann et al., 2009). It remains unclear whether the GICC05 age-scale appears to be too young (Fleitmann et al., 2009; Moseley et al., 2014) during the Marine Isotope Stages 3 (MIS 3) (Svensson et al., 2008; Skinner, 2008; Zhao et al., 2010). To further constrain the timing and spatial distribution of the millennial-scale climate variability, high-resolution and absolute-dated records are required from different climate regions. The teleconnections between the high latitude and tropic climate, which are considered as the underlying driver of the ASM variability, can also be deciphered (e.g., Wang et al., 2008; Landais et al., 2015; Chen et al., 2016).

Here, we report a new stalagmite record from the Dragon Cave in northern China, near the eastern boundary of the Chinese Loess Plateau, where very limited well-dated proxy records are currently available. High uranium contents of 0.4–1.2 ppm in the sample result in age uncertainties less than 0.4%, which allows us to accurately reconstruct the millennial-scale evolution of the East Asian summer monsoon (EASM) during MIS 3, especially from 53 to 38 ka BP. Three foci include (1) refinement of the timing, duration, and transition of Chinese Interstadials (CIS, that is strengthened Monsoon event, first defined in Cheng et al., 2006) 14–8, (2) clarification of an intensified ASM period at 48–38 ka BP and its possible forcings, and (3) examination of the relationship between these millennial-scale events as reconstructed in China and Greenland and evaluation of Greenland ice core chronology at MIS 3.

2. Study site

Dragon Cave (38°46′N, 113°16′E, at an elevation of 1600 m) is located in the semi-arid Shanxi Province, northern China, 60 km northeast of Changzhi City in the west flank of the Taihang Mountain (Fig. 1). The regional hydroclimate is strongly influenced by the Asian monsoon, and characterized by warm-wet summers and cool-dry winters. At the nearest meteorological station in Changzhi City, the monthly average surface air temperature (1970–2000) [Supplementary Fig. 1 (hereafter Fig. S1)] shows a minimum of −4.6 °C in January and a maximum of 22.5 °C in July with an annual mean of 9.9 °C. Annual mean precipitation is 530 mm, of which 68% falls between June and September when the ASM prevails.

The cave, 1000 m in length with an only entrance at the foot of the hill, is overlain by approximately 50-m Ordovician limestone (Qian, 1960). The largest chamber, where our stalagmite sample L30 was collected, is 20 m in height and 500 m away from the cave entrance. The relative humidity in this chamber is 98% as observed in summer 2014. Cave internal temperature of 10.3 °C matches annual mean ground temperature in the area. Dense forested vegetation, consisting primarily of temperate deciduous broad-leaved trees, covers the cave site and surrounding area.

3. Samples and methods

The columnar-shaped stalagmite L30 is 370 mm in length and its diameter ranges between 90 and 120 mm from top to bottom. After halved and polished, yellow clay bands are observed at depth intervals of 13–25 mm and 315–318 mm from the top, expressing some possible hiatuses (Fig. S2).

Thirty-one subsamples, 100–200 mg each, were drilled for U-Th chemistry (Shen et al., 2003), and ^{230}Th dating (Shen et al., 2002, 2012). Uranium-thorium isotopic measurements were performed on a multi-collection inductively coupled plasma mass spectrometer (MC-ICP-MS), Thermo Finnigan NEPTUNE, in the High-precision Mass Spectrometry and Environment Change Laboratory (HISPEC), Department of Geosciences, National Taiwan University (Shen et al., 2012). A gravimetrically calibrated (Cheng et al., 2013) triple-spike, ^{229}Th-^{233}U-^{236}U, isotope dilution method was employed to correct mass bias and determine U-Th contents and isotopic compositions (Shen et al., 2012). The half-lives of U-Th nuclides used are available in Cheng et al. (2013). Uncertainties in the U-Th isotopic data and ^{230}Th dates are calculated at the 2σ level or two standard deviations of the mean ($2\sigma_m$) unless otherwise noted.

For stable isotopic measurements, 380 subsamples, 10–20 μg each, were drilled with a 0.3 mm-diameter carbide dental burr at 1-mm intervals, except for two depth intervals of 63–83 mm and 160–191 mm, where the subsamples were drilled at 0.5-mm intervals. The traditional Hendy Test for isotopic equilibrium states that $\delta^{18}O$ should be nearly constant along a single growth layer and that $\delta^{13}C$ and $\delta^{18}O$ should not co-vary down the length of the growth axis (Hendy, 1971). Five coeval subsamples from three horizons were selected arbitrarily from stalagmite L30 and subjected to the "Hendy Test" (Hendy, 1971) to evaluate the oxygen isotopic equilibrium conditions during calcite precipitation. Oxygen isotopic analysis was conducted on a Finnigan-MAT 253 mass spectrometer equipped with an automatic Kiel Carbonate Device at the College of Geography Science, Nanjing Normal University. Carbonate $\delta^{18}O$ data are reported relative to the Vienna Pee Dee Belemnite (VPDB), and standardization was accomplished using NBS-19. Reproducibility of $\delta^{18}O$ values is ± 0.06‰ at the 1-sigma level.

4. Results and discussion

4.1. Chronology

Determined U-Th isotopic compositions and ^{230}Th dates of stalagmite L30 are shown in Table 1. Most (30/31) of $^{230}Th/^{232}Th$ atomic ratios are larger than 1×10^{-3}. It indicates that detrital Th content and the uncertainty for initial ^{230}Th correction are not significant. The corrected ^{230}Th dates are in a stratigraphic order and range from 53.2 ± 0.14 to 1.263 ± 0.005 ka BP. An age model was established based on linear interpolation between ^{230}Th dates. In addition, a chronology using StalAge (Scholz and Hoffmann, 2011) was constructed as well, and that it didn't significantly differ from our chronology using linear interpolation. As shown in Fig. 2, four growth hiatuses at depths of 15, 24, 46, and 63 mm from the top are identified. They are bounded by dates of 2.2 and 8.3 ka BP, 9.9 and 18.2 ka BP, 25.0 and 34.3 ka BP, 35.1 and 38.3 ka BP, respectively. The correspondent average temporal resolution is less than 66 yr at depths of 145–319 mm and 50–80 mm, ~100 yr at depths of 80–145 mm and 0–12 mm, and ~400 yr at the depth of 12–50 mm. The calculated growth rates range from the fastest value of 17 μm/yr at 53.3–38.3 ka BP to the lowest one of 3 μm/yr at 25.0–18.2 ka BP.

4.2. Dragon stalagmite L30 oxygen isotope record

Dragon L30 $\delta^{18}O$ values, ranging from −7.0‰ to −10.5‰, change dramatically throughout the entire record with an amplitude of over

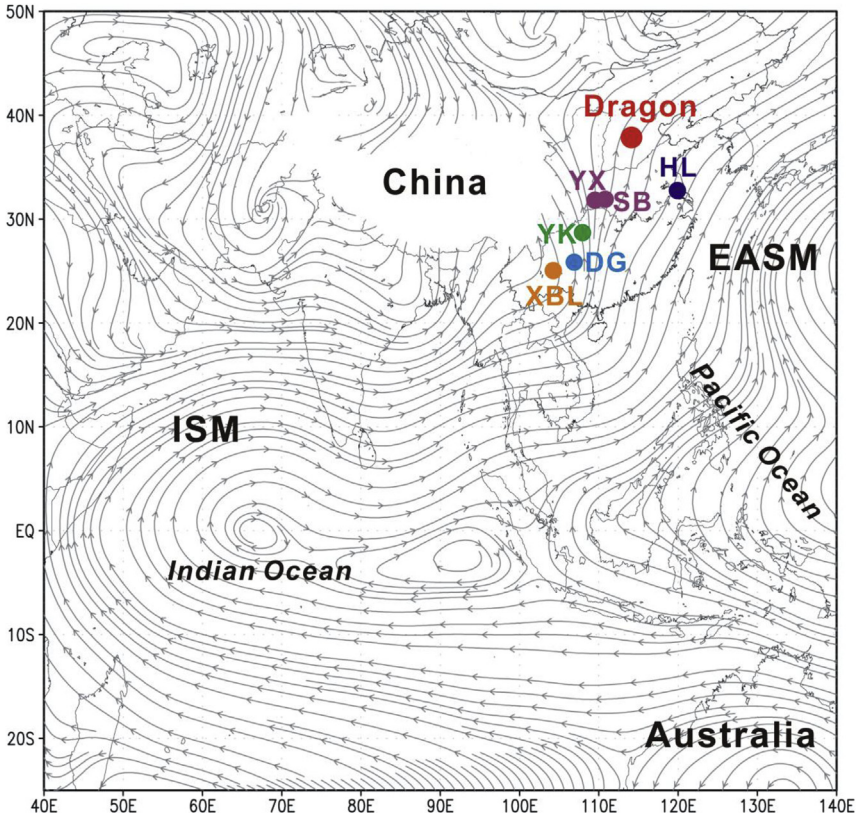

Fig. 1. Summer (June-July-August, JJA) mean 850 hPa streamline based on NCEP/NCAR Reanalysis during 1971–2000. Red dot is the location of Dragon Cave. The 'EASM' and 'ISM' denote the regions mainly influenced by the East Asian Summer Monsoon and the Indian Summer Monsoon, respectively. Locations of Yongxing (YX, Chen et al., 2016), Sanbao (SB, Wang et al., 2008; Dong et al., 2010), Hulu (HL, Wang et al., 2001), Yangkou (YK, Han et al., 2016), Dongge (DG, Dykoski et al., 2005), and Xiaobailong Caves (XBL, Cai et al., 2006) (dots) are also marked. (For interpretation of the references to color in this figure legend, the reader is referred to the Web version of this article.)

1‰ on millennial timescale during MIS 3. The lightest $\delta^{18}O$ values of −10.5 ~ −10.0‰ are observed during the early Holocene, while the heaviest of −7.0‰ is found at H1. The evolution of the L30 $\delta^{18}O$ record over the past 53 ka closely follows North Hemisphere summer insolation (NHSI) curve and agrees with data previously published from other Chinese caves (Wang et al., 2001; Dykoski et al., 2005; Dong et al., 2010; Chen et al., 2016) (Fig. 3).

Superimposed on the long-term evolution, the Dragon L30 $\delta^{18}O$ record is featured with a number of millennial-timescale strong and weak monsoon events. Six distinct positive anomalies in $\delta^{18}O$ centered respectively at 47.6, 43.6, 42.3, 39.0, 24.1 and 17.0 ka BP, reflecting weaker monsoon episodes with durations of approximately 1-kyr (Figs. 3 and 4). The weak monsoon event at 47.6 ka BP is indicated by a substantially abrupt positive shift of 1.1‰ in our $\delta^{18}O$ values within just 90-yr at the onset of the H5 event (Fig. 5). Six strong monsoon intervals occurred at 53.0, 49.2, 46.9, 43.5, 41.8, and 40.2 ka BP, respectively. On the sub-orbital scales, there is a decreasing trend of our $\delta^{18}O$ values from 48 to 38 ka BP. Similar feature is also apparent among data from previously published Chinese caves (Wang et al., 2001; Cai et al., 2006; Chen et al., 2016; Han et al., 2016) (Fig. 4).

4.3. Regional replication and interpretation of stalagmite $\delta^{18}O$

$\delta^{18}O$ and $\delta^{13}C$ data of coeval subsamples from three arbitrarily selected growth layers at 45 mm (25.0 ka BP), 143 mm (45.9 ka BP), and 250 mm (50.5 ka BP) are plotted in Fig. S3). Two-sigma variability of ± 0.06–0.12‰ for the coeval $\delta^{18}O$ data (Fig. S3a) and insignificant correlation (r^2 = 0.01–0.22) between $\delta^{18}O$ and $\delta^{13}C$ values (Fig. S3b) suggest that the oxygen data pass the Hendy Test (Hendy, 1971). Replication test (Dorale and Liu, 2009), involving the comparison of two or more speleothem records from different caves or different locations within the same cave that grew contemporarily, is another rigorous test for evaluating isotopic equilibrium conditions. Stalagmite L30 $\delta^{18}O$ record was compared with data of YX51 from Yongxing Cave (31°35′N, 111°14′E; Chen et al., 2016), and SB43 and SB3 from Sanbao Cave (31°40′N, 110°26′E; Dong et al., 2010; Wang et al., 2008) in central China, and MSD and YD from Hulu Cave (32°30′N, 119°10′E; Wang et al., 2001) in eastern China, and D4 from Dongge Cave (25°17′N, 108°05′E; Dykoski et al., 2005) in southwestern China (see Fig. 1 for cave locations). The $\delta^{18}O$ variations of all stalagmites are synchronous during their contemporaneous growth periods (Fig. 3b–d). This test further indicates that the variability of Chinese stalagmite $\delta^{18}O$ records is, at least, of regional significance.

Previous studies in southern China showed that changes in Chinese stalagmite $\delta^{18}O$ records mainly register variations in ASM intensity on decadal to orbital timescales (e.g., Wang et al., 2001, 2008; Yuan et al., 2004; Cheng et al., 2009). However, paleo-moisture and/or precipitation proxies and recent model simulations suggested that Chinese stalagmite $\delta^{18}O$ could mainly reflect changes in moisture sources and/or water vapor pathways and might not be considered as a reliable indicator of ASM intensity (Maher, 2008; LeGrande and Schmidt, 2009; Pausata et al., 2011; Liu et al., 2015). However, Cheng et al. (2016) clarified that ASM variations inferred by the stalagmite $\delta^{18}O$ may reflect a mean state of summer monsoon intensity and/or integrated moisture transports rather than the actual amount of local precipitation. A higher proportion of regional ASM rainfall and/or higher spatially integrated monsoon rainfall between the tropical monsoon sources and the caves would result in more negative stalagmite $\delta^{18}O$. This interpretation was supported by a recent model simulation (Liu et al., 2014) and an empirical study (Orland et al., 2015), which have suggested that local stalagmite records represent proxies of the EASM intensity in northern China.

Recently, a lake-level-inferred EASM intensity record from the Dali Lake, located 700 km north of the Dragon Cave, is highly correlated with Lianhua stalagmites $\delta^{18}O$ (Dong et al., 2015, 2018) on precessional and millennial timescales during the Holocene (see Fig. 3 of Goldsmith et al., 2017). Higher Dali lake levels correspond to more negative stalagmite $\delta^{18}O$, and vice versa. On the basis of this correlation and empirical and model studies (Liu et al., 2014; Orland et al., 2015), we interpret our Dragon Cave stalagmite $\delta^{18}O$ records as qualitative

Table 1
Uranium and thorium isotopic compositions and ^{230}Th ages for stalagmite L30 by MC- ICP-MS.

ID/	^{238}U	^{232}Th	δ^{234}U	^{230}Th/^{238}U	^{230}Th/^{232}Th	Age (ka BP)	Age (ka BP)	δ^{234}U
Depth (mm)	ppb	ppt	measured (‰)[a]	activity[c]	atomic (x 10^{-3})	uncorrected	corrected[c,d]	Initial (‰)[b]
L30-3	641.25 ± 0.71	306.0 ± 5.3	3916.0 ± 5.4	0.0596 ± 0.0002	2.059 ± 0.036	1.2657 ± 0.0048	1.2631 ± 0.0050	3930.7 ± 5.4
L30-12	804.0 ± 1.2	170.0 ± 5.1	3971.5 ± 8.1	0.1038 ± 0.0031	8.09 ± 0.34	2.233 ± 0.068	2.232 ± 0.068	3997.3 ± 8.2
L30-18	741.70 ± 0.87	3060.3 ± 8.9	3746.1 ± 5.1	0.3540 ± 0.0014	1.4147 ± 0.0068	8.310 ± 0.036	8.287 ± 0.038	3835.4 ± 5.3
L30-22	688.17 ± 0.67	8084 ± 152	3808.3 ± 4.6	0.4254 ± 0.0025	0.597 ± 0.012	9.923 ± 0.063	9.860 ± 0.070	3916.4 ± 4.8
L30-27	562.24 ± 0.58	200.0 ± 3.3	4111.6 ± 5.3	0.8029 ± 0.0017	37.211 ± 0.61	18.164 ± 0.046	18.162 ± 0.046	4328.6 ± 5.7
L30-38	645.32 ± 0.79	47.6 ± 2.4	4154.7 ± 6.3	0.9554 ± 0.0021	214 ± 11	21.700 ± 0.060	21.700 ± 0.060	4418 ± 6.7
L30-45	740.9 ± 2.5	79.7 ± 6.9	4139.4 ± 21.2	1.0856 ± 0.0043	166 ± 14	25.02 ± 0.16	25.02 ± 0.16	4443 ± 23
L30-50	473.23 ± 0.63	20.8 ± 4.4	3941.6 ± 7.1	1.3869 ± 0.0028	521 ± 110	34.32 ± 0.10	34.32 ± 0.10	4343.2 ± 7.9
L30-58	784.0 ± 2.3	24.9 ± 7.5	3938 ± 19	1.4023 ± 0.0052	728 ± 220	34.78 ± 0.21	34.78 ± 0.21	4345 ± 21
L30-63	690.3 ± 1.2	538.2 ± 6.9	3839.8 ± 9.0	1.4141 ± 0.0031	29.90 ± 0.39	35.09 ± 0.11	35.09 ± 0.11	4351 ± 10
L30-66	673.55 ± 0.71	616.3 ± 4.8	3811.5 ± 5.4	1.4853 ± 0.0032	26.77 ± 0.21	38.26 ± 0.11	38.25 ± 0.11	4246.7 ± 6.2
L30-67	1029.5 ± 1.8	69.2 ± 6.5	3829.8 ± 10.6	1.4914 ± 0.0035	366 ± 34	38.27 ± 0.14	38.27 ± 0.14	4267 ± 12
L30-79	434.16 ± 0.59	355.3 ± 3.5	3744.7 ± 6.2	1.5149 ± 0.0028	30.52 ± 0.30	39.78 ± 0.10	39.77 ± 0.10	4190.3 ± 7.1
L30-81	790.84 ± 0.85	402 ± 11	3750.7 ± 5.3	1.5307 ± 0.0029	49.7 ± 1. 4	40.20 ± 0.10	40.20 ± 0.10	4201.9 ± 6.1
L30-101	600.54 ± 0.71	34.5 ± 3.0	3692.3 ± 5.7	1.5870 ± 0.0032	455 ± 40	42.53 ± 0.12	42.53 ± 0.12	4163.9 ± 6.6
L30-120	788.2 ± 2.8	71.0 ± 6.6	3638.6 ± 20.7	1.6316 ± 0.0071	299 ± 28	44.53 ± 0.33	44.53 ± 0.33	4126.6.1 ± 23.8
L30-148	939.4 ± 1.8	260.1 ± 5.6	3639.0 ± 9.6	1.6846 ± 0.0036	100.3 ± 2.2	46.23 ± 0.16	46.23 ± 0.16	4147 ± 11
L30-162	881.0 ± 1.6	287.2 ± 4.7	3631.6 ± 9.4	1.6901 ± 0.0034	85.5 ± 1.4	46.50 ± 0.16	46.50 ± 0.16	4142 ± 11
L30-164	805.05 ± 0.91	323 ± 11	3637.1 ± 5.5	1.7132 ± 0.0035	70.3 ± 2.3	46.72 ± 0.13	46.71 ± 0.13	4194.8 ± 6.5
L30-166	522.20 ± 0.67	200.1 ± 3.1	3699.4 ± 6.5	1.7309 ± 0.0031	74.5 ± 1.2	47.00 ± 0.13	47.00 ± 0.13	4224.9 ± 7.5
L30-171	990.9 ± 1.8	338.8 ± 5.3	3594.9 ± 10.6	1.6969 ± 0.0037	81.8 ± 1,3	47.17 ± 0.18	47.17 ± 0.18	4107 ± 12
L30-179	770.8 ± 1.2	1051.5 ± 5.5	3474.0 ± 7.2	1.6649 ± 0.0034	20.12 ± 0.11	47.61 ± 0.15	47.61 ± 0.15	3974.3 ± 8.4
L30-185.5	919.6 ± 1.1	2332 ± 11	3596.3 ± 5.2	1.7240 ± 0.0032	11.209 ± 0.053	48.05 ± 0.12	48.04 ± 0.12	4119.2 ± 6.1
L30-186	896.3 ± 4.4	296.6 ± 7.0	3620 ± 29	1.7370 ± 0.0093	95.2 ± 2.5	48.18 ± 0.47	48.18 ± 0.47	4147.8 ± 33.5
L30-190	738.3 ± 1.1	497.7 ± 7.1	3526.3 ± 7.4	1.7050 ± 0.0034	41.70 ± 0.60	48.30 ± 0.15	48.30 ± 0.15	4042.0 ± 8.6
L30-210	890.6 ± 3.1	255.4 ± 6.9	3607 ± 18	1.7652 ± 0.0073	101.5 ± 2.8	49.27 ± 0.34	49.27 ± 0.34	4146.4 ± 21.9
L30-223	970.3 ± 1.2	248.7 ± 7.0	3580.2 ± 6.4	1.7785 ± 0.0031	114.4 ± 3.2	50.08 ± 0.13	50.07 ± 0.13	4124.4 ± 7.5
L30-245	944.8 ± 5.4	341.9 ± 6.8	3534 ± 31	1.7668 ± 0.0110	80.5 ± 1.6	50.29 ± 0.56	50.29 ± 0.56	4073.9 ± 36.5
L30-297	1157.1 ± 1.3	100.7 ± 3.5	3462.5 ± 5.2	1.8016 ± 0.0030	341 ± 12	52.50 ± 0.13	52.50 ± 0.13	4016.1 ± 6.2
L30-315	505.51 ± 0.68	213.1 ± 3.5	3457.3 ± 6.4	1.8199 ± 0.0031	71.3 ± 1.2	53.22 ± 0.14	53.22 ± 0.14	4018.3 ± 7.6
L30-315	730.80 ± 0.93	8991 ± 24	3410.2 ± 6.1	1.8031 ± 0.0052	2.4164 ± 0.0091	53.32 ± 0.21	53.26 ± 0.21	3963.9 ± 7.5

Analytical errors are 2σ of the mean.

[a] $\delta^{234}U = ([^{234}U/^{238}U]_{activity} - 1) \times 1000$.

[b] δ^{234}U corrected was calculated based on ^{230}Th age (T), i.e., $\delta^{234}U_{initial} = \delta^{234}U_{measured} \times e^{\lambda 234 * T}$, T is corrected age.

[c] $[^{230}Th/^{238}U]_{activity} = 1 - e^{-\lambda 230 T} + (\delta^{234}U_{measured}/1000)[\lambda_{230}/(\lambda_{230} - \lambda_{234})](1 - e^{-(\lambda 230 - \lambda 234) T})$, where T is the age.

[d] Age (before 1950 AD) corrections were made using a ^{230}Th/^{232}Th atomic ratio of $4 \pm 2 \times 10^{-6}$, which is value for material at secular equilibrium with the crustal ^{232}Th/^{238}U value of 3.8 and arbitrarily assumed uncertainty of 50%.

proxies for regional precipitation and the intensity of the EASM in northern China, with more (less) negative values indicating a stronger (weaker) EASM. A comparison of the Dragon L30 δ^{18}O data and a quantitatively proxy inferred summer rainfall record in the western Chinese Loess Plateau during the last glacial period (Rao et al., 2013) is given in Fig. 3a and b. During the period of 50–10 ka BP, the two time series correlate well with regards to both the trend and variation. For example, strongly negative δ^{18}O values in L30 record match intensified summer monsoon precipitation in the loess record for DO 14–8 events. For the H events 5, 4, 2 and 1, the relatively positive δ^{18}O values are concurrent with the decreased summer monsoon precipitation. This agreement further supports our hydroclimatic interpretation of the Dragon L30 data.

4.4. Coherence of the regional monsoon changes over the entire Asian Monsoon territory during MIS 3

To better understand the regional nature of the ASM variability and its forcings during the last glacial period, we compared Dragon record to precisely-dated contemporaneous speleothem data from other caves in different monsoonal regions, including Sanbao (Wang et al., 2008; Dong et al., 2010), Yongxing (Chen et al., 2016) and Hulu (Wang et al., 2001) in the EASM zone (Fig. 3), and also Dongge (Dykoski et al., 2005), Yangkou (Han et al., 2016) and Xiaobailong (Cai et al., 2006) in southwestern Indian summer monsoon zone (Figs. 3d and 4). On orbital scales, there is a general agreement among δ^{18}O records between Dragon and other Chinese caves (Figs. 1 and 3b–d). For example, the strongest EASM occurred at the early-middle Holocene; while, the weakest monsoon happened during the H1, which is characterized by the largest difference of 4–5‰ among δ^{18}O records at the transition of the last glacial-interglacial period. The consistence among different caves indicates that the first-order similar climatic forcing is original from NHSI over the whole monsoonal China (Wang et al., 2001, 2008; Cheng et al., 2016) (Fig. 3b).

4.5. 53–38-ka interval and CIS 14–8 events

As illustrated in Fig. 4, seven distinct millennial-scale negative excursions in L30 δ^{18}O record show strong monsoon events CIS 14–8 in northern China. The CIS events 13, 12, 11, 10 and 9 initiated at 49.2, 46.9, 43.5, 41.8 and 40.2 ka BP, respectively, except for the CIS 14 with a hiatus at its initiation in L30 record. The CIS 8 is partly documented and its onset is clearly identified at 38.3 ka BP. These millennial-scale strong monsoon events are also observed in other Chinese caves, such as Hulu (Fig. 4d, Wang et al., 2001), Yongxing (Fig. 4c, Chen et al., 2016), Yangkou (Fig. 4e, Han et al., 2016), and Xiaobailong (Fig. 4f, Cai et al., 2006). This agreement indicates the concurrence of these strong millennial-scale ASM events in entire monsoonal China. In addition, all Chinese stalagmite records are concurrent with the DO 14–8 in terms of the timing and duration within their respective chronological uncertainties (Fig. 4).

Two prominent weak EASM anomalies correlate well with the North Atlantic IRD events H5 and H4 (Bond et al., 1993), and their counterparts can also be found in NGRIP records (Fig. 4a). The good alignments

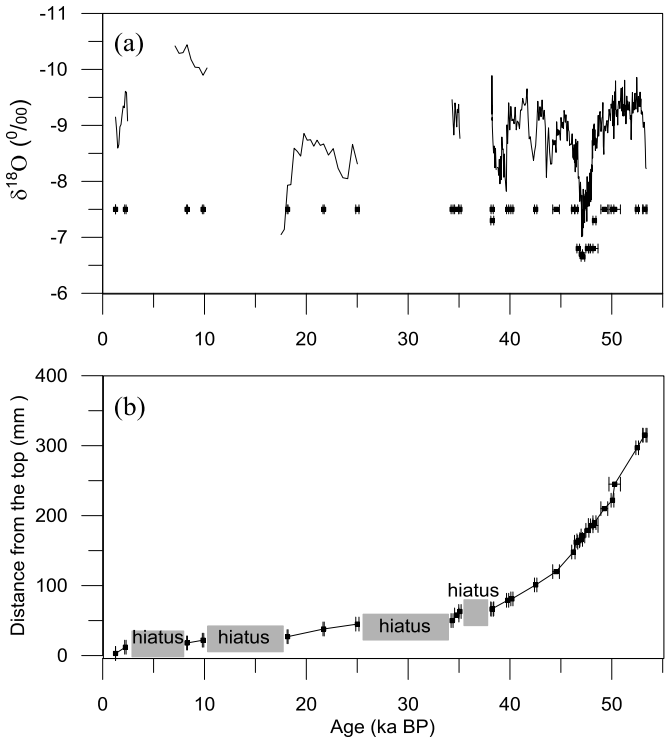

Fig. 2. (a) Stalagmite L30 $\delta^{18}O$ record. **(b)** U-Th age with 2σ uncertainty (Table 1) versus depth for stalagmite L30.

between the CIS in China and DO events in Greenland, and between weak EASM events in China and the IRD events in North Atlantic support the previous hypothesis that the millennial-scale abrupt climate changes in North Atlantic region may influence the East Asian monsoonal climate by the reorganization of large-scale atmospheric circulation patterns (Porter and An, 1995; Wang et al., 2001). Changes in large-scale atmospheric circulations are linked to the intertropical convergence zone (ITCZ) shifts providing a potential association between the observed millennial-scale co-variation in the low-latitude regions (EASM) and high latitudes (North Atlantic) (Wang et al., 2001; Fleitmann et al., 2007).

Despite the above similarities at millennial timescales, there are some considerable and apparent differences between the ASM and Greenland ice-core records (Fig. 4). For example, the interval between 48 and 38 ka BP, which corresponds to gradual cooling conditions in Greenland, is characterized by a trend towards more negative $\delta^{18}O$ values in the L30 record, suggesting enhanced monsoon conditions over the 10 ka. Other speleothem records from the ASM region also show a distinct trend towards more negative $\delta^{18}O$ values during this interval of MIS3 (Fig. 4c–f). The only exception with a slightly inverse trend expressed in Hulu record (Wang et al., 2001) (Fig. 4d) implies possible heterogeneity of regional monsoon dynamics, which should be further clarified with more records from Nanjing. During DO 12, Greenland ice core $\delta^{18}O$ values increased abruptly and then decreased gradually. On the contrast, the CIS 12 in the L30 record began with a stepwise decrease in $\delta^{18}O$ values at 47.0–45.5 ka BP and finally ended up with a gradual increase in $\delta^{18}O$ values at 45.3–44.0 ka BP, making an approximate isosceles triangle pattern. The symmetrical features are also presented in other high temporal resolution cave records (Fig. 4c–e), but slightly different from the Xiaobailong record (Cai et al., 2006) (Fig. 4f). This apparent mismatch between $\delta^{18}O$ values in the Greenland and those from the ASM region suggests that additional forcing(s), not originally from the northern high latitudes, may modulate the variability of the ASM (An et al., 2011; Cai et al., 2006; Rohling et al., 2009; Caley et al., 2013; Han et al., 2016).

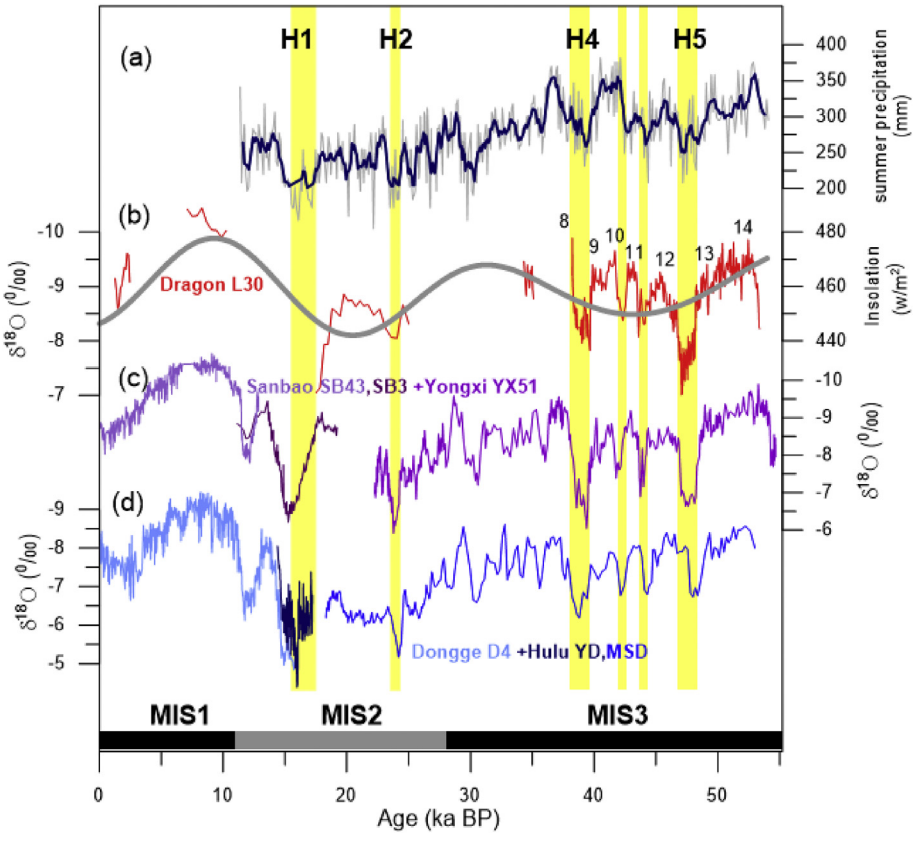

Fig. 3. A comparison of stalagmite $\delta^{18}O$ and Loess records. **(a)** Quantitative reconstruction of summer rainfall in the western Chinese Loess Plateau, north China (Rao et al., 2013). **(b)** Dragon L30 $\delta^{18}O$ record (red line, this study), followed by the North Hemisphere Insolation at 33°N (gray curve) (Berger, 1978). **(c)** Spliced stalagmite $\delta^{18}O$ records from Sanbao (SB43, twilight violet; SB3, plum; Wang et al., 2008; Dong et al., 2010) and Yongxing Caves (YX52, purple, Chen et al., 2016). **(d)** Spliced stalagmite $\delta^{18}O$ records from Dongge (D4, baby blue, Dykoski et al., 2005) and Hulu Caves (YD, dark navy blue; MSD, blue; Wang et al., 2001). Light yellow bars represent weakened ASM periods at Heinrich (H) events, demonstrated by the North Atlantic Ocean sediments (Heinrich, 1988; Bard et al., 2000). Numbers denote CIS events. (For interpretation of the references to color in this figure legend, the reader is referred to the Web version of this article.)

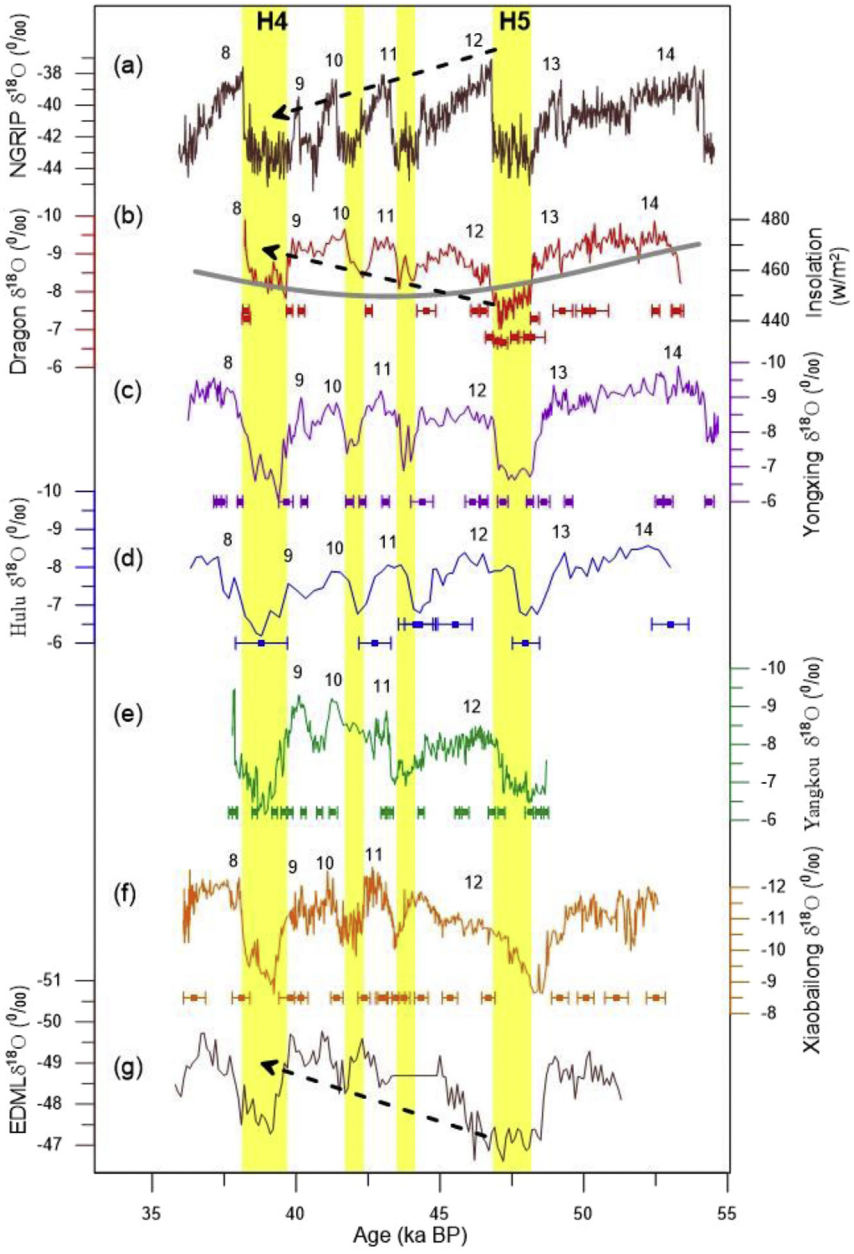

Fig. 4. A comparison of ice core and stalagmite $\delta^{18}O$ time series along a latitudinal transect from the South Hemisphere to North Hemisphere. **(a)** NGRIP ice record on GICC05 timescale (NorthGRIP-community-members, 2004; Svensson et al., 2008). Stalagmite $\delta^{18}O$ records are from caves of **(b)** Dragon (this study) in northern China, **(c)** Yongxing in central China (Chen et al., 2016), **(d)** Hulu (Wang et al., 2001) in eastern China, and **(e)** Yangkou (Han et al., 2016) and **(f)** Xiaobailong (Cai et al., 2006) in southwestern China. **(g)** Antarctica EDML ice record on GICC05 timescale (EPICA community Members, 2006). ^{230}Th ages with errors are color-coded by stalagmite. Light yellow bars denote weakened ASM periods in Dragon record. Gray curve in **(b)** is North Hemisphere Insolation at 33°N (Berger, 1978). Numbers denote CIS and DO events. Arrows shows the multi-millennial trend of the decreasing Greenland and Antarctic air temperatures and increasing ASM circulation, respectively. (For interpretation of the references to color in this figure legend, the reader is referred to the Web version of this article.)

4.6. Forcings for strengthening ASM from 48 to 38 ka BP

Recent meteorological studies indicate that the large portion of the moisture source of the ASM is originated from the oceans in the Southern Hemisphere and transported by the cross-equatorial flows through the Southern China Sea (Liu et al., 2014; Xue et al., 2004) (Fig. 1). Southern Hemisphere cooling may have intensified boreal summer monsoons on centennial-millennial timescales (Rohling et al., 2009; An et al., 2011; Caley et al., 2013; Chen et al., 2016). The monsoon-related inter-hemisphere latent heat transfer could explain the anomalously long duration of DO or CIS events that coincides with marked Antarctic cooling event, especially interstadials 12, 8 and 1 (Rohling et al., 2003; EPICA community Members, 2006; Cai et al., 2006; Shen et al., 2010; Chen et al., 2016). The inter-hemispheric temperature gradient obviously increases when one hemisphere becomes colder and the other becomes warmer, which could push the ITCZ into the warmer hemisphere (Chiang and Friedman, 2012). During the period of CIS 12–8, the gradual cooling of the Antarctic in Fig. 4g could strengthen the Mascarene and Australian highs, which finally drove a strong "push" (An et al., 2011) cross-equatorial flow and induced an intensified ASM across the monsoonal China (Wang and Xue, 2003; Xue et al., 2004). The enhanced cross-equatorial flow could be accompanied by a slowly northward movement of the ITCZ and an expansion of the cold tongue in the eastern Pacific Ocean as the southeast trade winds intensified and the northeast trade winds weakened (Peterson et al., 2000). The symmetric Hadley cell became asymmetric, with the rising branch of Hadley circulation shifted northward. The variability of the ASM is also closely coupled to the low-latitude oceanic condition. As shown in Fig. 4, a clear cooling trend is expressed in the North high-latitude region from 48 to 38 ka BP; instead, the summer insolation at 33°N gradually increased over this period. In Asian monsoon realm, cooling oceans and warming continent by increasing of summer insolation can enhance the land-sea temperature contrast and strengthen the ASM. These processes could cause more moisture to converge into the Asian monsoon realm and the intensified ASM.

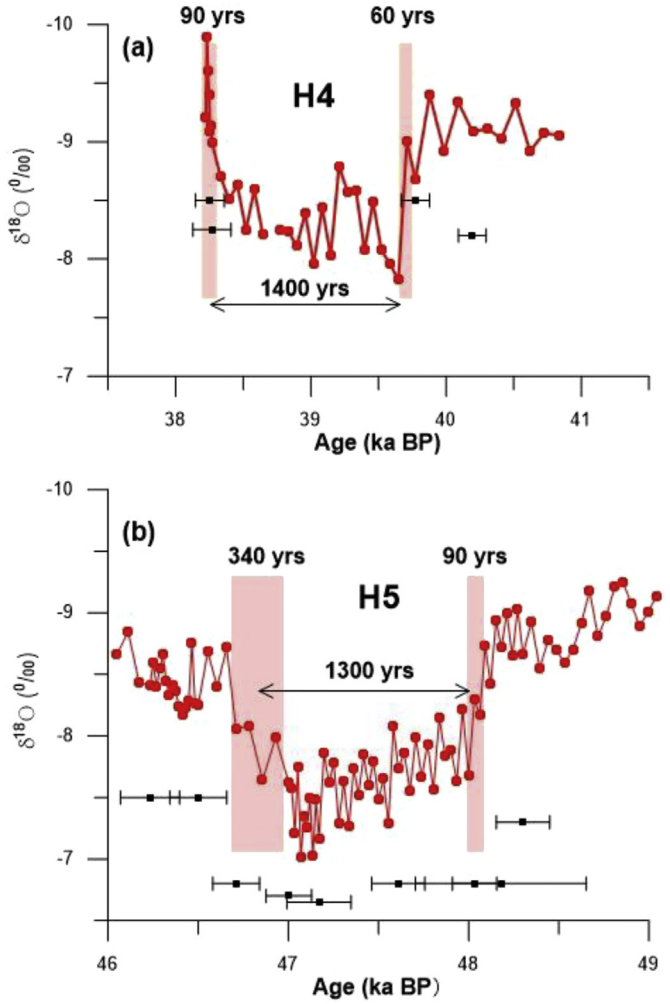

Fig. 5. The timing and structure of weak Asian summer monsoon at **(a)** H4 and **(b)** H5 events registered in Dragon L30 $\delta^{18}O$ record. Pink columns denote the onsets and terminations with the durations for two distinct weak monsoon events, respectively. ^{230}Th ages with 2σ errors are given by record. (For interpretation of the references to color in this figure legend, the reader is referred to the Web version of this article.)

4.7. Heinrich events 5 and 4

H events were identified by the massive surges and melts of icebergs in the North Atlantic, perturbing the global ocean circulation and triggering a slowdown or shutdown of the North Atlantic Meridional Overturning Circulation (Heinrich, 1988; Bard et al., 2000). Such climate signals of cold/arid anomalies around the North Atlantic can be transmitted into the Asian interior via atmospheric teleconnections (Porter and An, 1995). Stalagmite records show that the ASM intensity could be synchronously decreased during H events (Wang et al., 2001; Zhao et al., 2010). During the MIS 3, Dragon L30 $\delta^{18}O$ record clearly illustrates weakened EASM events during H 5 and H 4, which are centered at 47.6 and 39.0 ka BP, respectively (Fig. 4).

The sudden onset of a weak EASM, accompanied by an abrupt enrichment of 1.2‰ in ^{18}O during the H4, spanned from 39.71 to 39.65 ka BP, and lasted for 60 years. The 90-yr recovery period was from 38.33 to 38.24 ka BP (Fig. 5a). The maximum $\delta^{18}O$ value of −7.8‰ was observed at 39.65 ka BP, and subsequently got slowly depleted during the 1400-yr H4. The corresponding weak EASM of H5 also showed an abrupt onset transition of 1.1‰ in the L30 $\delta^{18}O$ record, lasting from 48.09 to 48.0 ka BP, and was only 90 yrs long (Fig. 5b). In contrast, the termination of the H5, from 47.0 to 46.66 ka BP, lasted about 340 years. The maximum $\delta^{18}O$ value of −7.0‰ was observed at 47.2 ka BP at the end of the 1300-yr H5. If the North Atlantic Meridional Overturning Circulation disturbance acts as a trigger for the H events, the rapid EASM decline during the early H5 and H4 suggests a significant reduction in the oceanic conveyor. Indeed, as shown in Fig. S4, the Atlantic Ocean circulation estimated by ^{231}Pa and ^{230}Th records (Henry et al., 2016) exhibited a significant decline during the early H events. This good consistence indicates a potential tight link between them.

Dragon L30 $\delta^{18}O$ record anchors the onset and termination of the H4 at 39.68 ± 0.11 and 38.29 ka ± 0.10 ka BP, and the H5 at 48.06 ± 0.15 and 46.88 ± 0.15 ka BP, respectively. These dates are consistent in the timing and transition with previously published stalagmite-inferred ASM changes across the monsoonal China within their respective dating errors (Fig. 4). In addition, the onset and end of the H4 in GICC05 chronology, at 39.85 ± 1.45 and 38.17 ± 1.57 ka BP, the H5 at 48.29 ± 1.99 and 46.81 ± 1.90 ka BP, respectively (Svensson et al., 2008; Rasmussen et al., 2014), match ones in Dragon L30 record. A detailed comparison of the Chinese stalagmite-recorded CIS events 13–8 with the corresponding Greenland DO events shows the absence of significant offsets between the Chinese stalagmite and the NGRIP $\delta^{18}O$ records from 50 to 38 ka BP (Fig. 6). This consistency between low-latitude and high-latitude climate dynamics supports the accuracy of ice core GICC05 chronology and indicates the strong hemispheric connection at millennial-scales.

5. Conclusions

Based on 31 precise ^{230}Th dates, we provide a high-resolution Asian monsoon record between 53.2 and 1.3 ka BP, especially from 53.2 to 38.0 ka BP, from the Dragon Cave, northern China. Our $\delta^{18}O$ records feature seven stronger monsoon intervals of CIS 14–8 associated with the corresponding DO events and four weak monsoon events linked to cold episodes in Greenland and ice-rafting events in the North Atlantic (i.e., H5, H4, H2 and H1). Our results are broadly consistent with previously published stalagmite $\delta^{18}O$ records from central and southern China, suggesting a synchronous change of the millennial-scale ASM events linked to the North Atlantic climate across the monsoonal China. The gradually strengthened ASM from 48 to 38 ka BP across the monsoonal China suggests an important role of Southern Hemisphere cooling and the enhanced land-sea temperature contrast due to rising summer insolation on the ASM on millennial scales during the period of MIS 3. There are no systematic age offsets between the Chinese

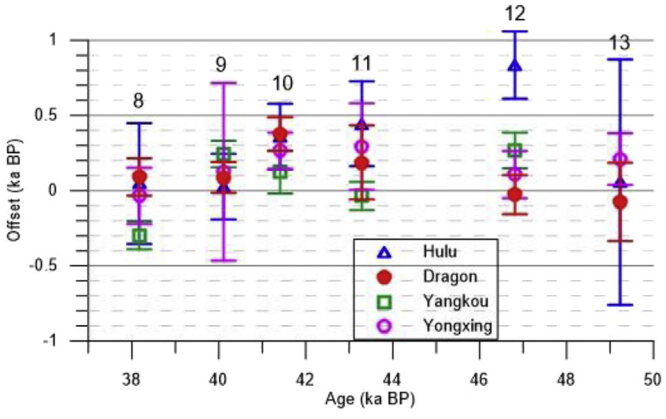

Fig. 6. Age offsets of Chinese stalagmite CIS events in different caves from their corresponding DO events under NGRIP chronology (Svensson et al., 2008) during 50–38 ka BP. Offset data are for caves of Dragon (this study, red), Yongxing (purple, Chen et al., 2016), Yangkou cave (green, Han et al., 2016), and Hulu (blue, Wang et al., 2001). Numbers denote CIS events. (For interpretation of the references to color in this figure legend, the reader is referred to the Web version of this article.)

stalagmite and the NGRIP $\delta^{18}O$ records from 50 to 38 ka BP, supporting the accuracy of ice core GICC05 chronology.

Author contribution

All authors in the manuscript have been involved with the work and agreed to its submission. There is no conflict of interest of any authors in relation to the submission. All authors contributed to discussion, interpretation of the results and writing of the revised manuscript. This paper has not been submitted elsewhere for consideration of publication.

Acknowledgements

We thank Dr. Shaohua Yang and Ms. Guifu Ao for their help with the field work and isotope analyses. Thanks are also given to two anonymous reviewers for his/her critical and instructive comments. Yin Jianjun is thanked for help with plotting Fig. 1. This research was supported by grants from the National Natural Science Foundation (NSFC, 41472317 to Dong, J.G., and 41672164 to Kong, X.G.), Jiangsu Overseas Research and Training Program for University Prominent Young and Middle-aged Teachers and Presidents, and the research opportunities fund of University of Sussex. Funding was also provided by grants from Taiwan ROC MOST (105-2119-M-002-001, 106-2628-M-002-013, to C.-C.S.) and the National Taiwan University (105R7625 to C.-C.S.).

Appendix A. Supplementary data

Supplementary data related to this article can be found at http://dx.doi.org/10.1016/j.quageo.2018.05.012.

References

An, Z., Clemens, S.C., Shen, J., Qiang, X., Jin, Z., Sun, Y., Prell, W.L., Luo, J., Wang, S., Xu, H., Cai, Y., Zhou, W., Liu, X., Liu, W., Shi, Z., Yan, L., Xiao, X., Chang, H., Wu, F., Ai, L., Lu, F., 2011. Glacial-interglacial indian summer monsoon dynamics. Science 333, 719–723.

Bard, E., Rostek, F., Turon, J.L., Gendreau, S., 2000. Hydrological impact of Heinrich events in the subtropical Northeast Atlantic. Science 289, 1321–1324.

Berger, A.L., 1978. Long-term variations of caloric insolation resulting from the Earth's orbital elements. Quat. Res. 9, 139–167.

Blunier, T., Brook, E.J., 2001. Timing of millennial-scale climate change in Antarctica and Greenland during the last glacial period. Science 291, 109–112.

Bond, G., Broecker, W., Johnsen, S., McManus, J., Labeyrie, L., Jouzel, J., Bonani, G., 1993. Correlations between climate records from North Atlantic sediments and Greenland ice. Nature 365, 143–147.

Broecker, W.S., 1998. Paleocean circulation during the Last Deglaciation: a bipolar seesaw? Paleoceanography 13, 119–121.

Burns, S.J., Fleitmann, D., Matter, A., Kramers, J., Al-Subbary, A.A., 2003. Indian ocean climate and an absolute chronology over Dansgaard/Oeschger events 9 to 13. Science 301 (5638), 1365–1367.

Cai, Y., An, Z., Cheng, H., Edwards, L.R., Kelly, M.J., Liu, W., Wang, X., Shen, C.C., 2006. High-resolution absolute-dated indian monsoon record between 53 and 36 ka from Xiaobailong Cave, southwestern China. Geology 34, 621–624.

Caley, T., Zaragosi, S., Bourget, J., Martinez, P., Malaizé, B., Eynaud, F., Rossignol, L., Garlan, T., Ellouz-Zimmermann, N., 2013. Southern Hemisphere imprint for Indo-Asian summer monsoons during the last glacial period as revealed by Arabian Sea productivity records. Biogeosciences 10, 7347–7359.

Chen, S.T., Wang, Y.J., Cheng, H., Edwards, R.L., Wang, X.F., Kong, X.G., Liu, D.B., 2016. Strong coupling of Asian Monsoon and Antarctic climates on suborbital timescales. Sci. Rep. 6, 32995.

Cheng, H., Edwards, R.L., Wang, Y.J., Kong, X.G., Ming, Y.F., Gallup, C.D., Kelly, M.J., Wang, X.F., Liu, W.G., 2006. A penultimate glacial monsoon record from Hulu Cave and two-phase glacial terminations. Geology 34, 217–220.

Cheng, H., Edwards, R.L., Broecker, W.S., Denton, G.H., Kong, X.G., Wang, Y.J., Zhang, R., Wang, X.F., 2009. Ice age terminations. Science 326, 248–252.

Cheng, H., Edwards, R.L., Shen, C.-C., Polyak, V.J., Asmerom, Y., Woodhead, J., Hellstrom, J., Wang, Y.J., Kong, X.G., Spötl, C., Wang, X.F., Alexander, E.C., 2013. Improvements in ^{230}Th dating, ^{230}Th and ^{234}U half-life values, and U-Th isotopic measurements by multi-collector inductively coupled plasma mass spectrometry. Earth Planet Sci. Lett. 372, 82–91.

Cheng, H., Edwards, R.L., Sinha, A., Spötl, C., Yi, L., Chen, S.T., Kelly, M., Kathayat, G., Wang, X.F., Li, X.L., Kong, X.G., Wang, Y.J., Ning, Y.F., Zhang, H.W., 2016. The Asian monsoon over the past 640,000 years and ice age terminations. Nature 534, 640–646.

Chiang, J.C.H., Friedman, A.R., 2012. Extratropical cooling cooling, Interhemispheric thermal gradients, and tropical climate change. Annu. Rev. Earth Planet Sci. 40, 383–412.

Dansgaard, W., Johnsen, S.J., Clausen, H.B., Dahl-Jensen, D., Gundestrup, N.S., Hammer, C.U., Hvidberg, C.S., Steffensen, J.P., Sveinjörnsdottir, a.e., Jouzel, J., Bond, G., 1993. Evidence for general instability of past climate from a 250-kyr ice core record. Nature 364, 218–220.

Dong, J.G., Wang, Y.J., Cheng, H., Hardt, B., Edwards, R.L., Kong, X.G., Wu, J.Y., Chen, S.T., Liu, D.B., Jiang, X.Y., Zhao, K., 2010. A high-resolution stalagmite record of the Holocene East Asian monsoon from Mt Shennongjia, central China. Holocene 20, 257–264.

Dong, J.G., Shen, C.C., Kong, X.G., Jiang, X.Y., 2015. Reconciliation of hydroclimate sequences from Loess Plateau and low-latitude zones in the East Asian monsoon territory over the past 14,500 years. Palaeogeogr. Palaeoclimatol. Palaeoecol. 435, 127–135.

Dong, J.G., Shen, C.C., Kong, X.G., Wu, C.-C., Hu, H.-M., Ren, H.J., Wang, Y., 2018. Rapid retreat of the East Asian summer monsoon in the middle Holocene and a millennial weak monsoon interval at 9 ka in northern China. J. Asian Earth Sci. 151, 31–39.

Dorale, J., Liu, Z.H., 2009. Limitations of Hendy Test criteria in judging the paleoclimatic suitability of speleothems and the need for replication. J. Cave Karst Stud. 71, 73–80.

Duan, F.C., Liu, D.B., Cheng, H., Wang, X.F., Wang, Y.J., Kong, X.G., Chen, S.T., 2014. A high resolution monsoon record of millennial-scale oscillations during Late MIS 3 from Wulu Cave, south-west China. J. Quat. Sci. 29, 83–90.

Dykoski, C.A., Edwards, R.L., Cheng, H., Yuan, D., Cai, Y., Zhang, M., Lin, Y., Qing, J., An, Z., Revenaugh, J., 2005. A high-resolution, absolute-dated Holocene and deglacial Asian monsoon record from Dongge Cave, China. Earth Planet Sci. Lett. 233, 71–86.

EPICA community Members, 2006. One-to-one coupling of glacial climate variability in Greenland and Antarctica. Nature 444, 195–197.

Fleitmann, D., Burns, S.J., Mangini, A., Mudelsee, M., Kramers, J., Villa, I., Neff, U., Al-Subbary, A.A., Buettner, A., Hippler, D., Matter, A., 2007. Holocene ITCZ and Indian monsoon dynamics recorded in stalagmites from Oman and Yemen (Socotra). Quat. Sci. Rev. 26, 170–188.

Fleitmann, D., Cheng, H., Badertscher, S., Edwards, R.L., Mudelsee, M., Göktürk, O.M., Fankhauser, A., Pickering, R., Raible, C.C., Matter, A., Kramers, J., Tüysüz, O., 2009. Timing and climatic impact of Greenland interstadials recorded in stalagmites from northern Turkey. Geophys. Res. Lett. 36, L19707.

Genty, D., Blamart, D., Ouahdi, R., Gilmour, M., Baker, A., Jouzel, J., Van-Exter, S., 2003. Precise dating of Dansgaard-Oeschger climate oscillations in western Europe from stalagmite data. Nature 421, 833–837.

Goldsmith, Y., Broecker, W.S., Xu, H., Polissar, P.J., deMenocal, P.B., Porat, N., Lan, J.H., Cheng, P., Zhou, W.J., An, Z.S., 2017. Northward extent of East Asian monsoon covaries with intensity on orbital and millennial timescales. Proc. Natl. Acad. Sci. U. S. A. 114, 1817–1821.

Han, L.Y., Li, T.Y., Cheng, H., Edwards, R.L., Shen, C.-C., Li, H.C., Huang, C.X., Li, J.Y., Yuan, N., Wang, X.B., Zhang, T.T., Zhao, X., 2016. Potential influence of temperature changes in the Southern Hemisphere on the evolution of the Asian summer monsoon during the last glacial period. Quat. Int. 392, 239–250.

Heinrich, H., 1988. Origin and consequences of cyclic ice rafting in the Northeast Atlantic Ocean during the past 130,000 years. Quat. Res. 29, 142–152.

Hemming, S.R., 2004. Heinrich events: massive late Pleistocene detritus layers of the North Atlantic and their global climate imprint. Rev. Geophys. 42, RG1005. http://dx.doi.org/10.1029/2003RG000128.

Hendy, C.H., 1971. The isotopic geochemistry of speleothems-I. The calculation of the effects of different modes of formation on the isotopic composition of speleothems and their applicability as palaeoclimatic indicators. Geochim. Cosmochim. Acta 35, 801–824.

Henry, L.G., McManus, J.F., Curry, W.B., Roberts, N.L., Piotrowski, A.M., Keigwin, L.D., 2016. North Atlantic ocean circulation and abrupt climate change during the last glaciations. Science 353, 470–474.

Kanner, L.C., Burns, S.J., Cheng, H., Edwards, R.L., 2012. High-latitude forcing of the South American summer monsoon during the last glacial. Science 335, 570–573.

Landais, L., Masson-Delmotte, V., Stenni, B., Selmo, E., Roche, D.M., Jouzel, J., Lambert, F., Guillevic, M., Bazin, L., Arzel, O., Vinter, B., Gkinis, V., Popp, T., 2015. A review of the bipolar seesaw from synchronized and high resolution ice core water stable isotope records from Greenland and East Antarctica. Quat. Sci. Rev. 114, 18–32.

LeGrande, A.N., Schmidt, G.A., 2009. Sources of Holocene variability of oxygen isotopes in paleoclimate archives. Clim. Past 5, 441–455.

Liu, Z.Y., Wen, X.Y., Brady, E.C., Otto-Bliesner, B., Yu, G., Lu, H.Y., Cheng, H., Wang, Y.J., Zheng, W.P., Ding, Y.H., Edwards, R.L., Cheng, J., Liu, W., Yang, H., 2014. Chinese cave records and the East Asia summer monsoon. Quat. Sci. Rev. 83, 115–128.

Liu, J.B., Chen, J.H., Zhang, X.J., Li, Y., Rao, Z.G., Chen, F.H., 2015. Holocene East Asian summer monsoon records in northern China and their inconsistency with Chinese stalagmite $\delta^{18}O$ records. Earth Sci. Rev. 148, 194–208.

Maher, B.A., 2008. Holocene variability of the East Asian summer monsoon from Chinese cave records: a re-assessment. Holocene 18, 861–866.

Meese, D.A., Gow, A.J., Alley, R.B., Grootes, P.M., Ram, M., Taylor, K.C., Zielinski, G.A., Bolzan, J.F., Mayewski, P.A., Waddington, E.D., 1997. The Greenland ice sheet project 2 depth-age scale: methods and results. J. Geophys. Res. 102, 26411–26423.

Moseley, G.E., Spötl, C., Svensson, A., Cheng, H., Brandstätter, S., Edwards, R.L., 2014. Multi-speleothem record reveals tightly coupled climate between central Europe and Greenland during Marine Isotope Stage 3. Geology 42, 1043–1046.

NorthGRIP-community-members, 2004. High-resolution record of Northern Hemisphere climate extending into the last interglacial period. Nature 431, 147–151.

Orland, I.J., Edwards, R.L., Cheng, H., Kozdon, R., Mellissa, C., Valley, J.W., 2015. Direct measurements of deglacial monsoon strength in a Chinese stalagmite. Geology 43, 555–558.

Pausata, F., Battisti, D., Nisancioglu, K., Bitz, C., 2011. Chinese stalagmite $\delta^{18}O$ controlled by changes in the Indian monsoon during a simulated Heinrich event. Nat. Geosci. 4, 474–480.
Peterson, L.C., Haug, G.H., Hughen, K.A., Röhl, U., 2000. Rapid changes in the hydrologic cycle of the tropical Atlantic during the last glacial. Science 290, 1947–1951.
Pierrehumbert, R.T., 2000. Climate change and the tropical Pacific: the sleeping dragon wakes. Proc. Natl. Acad. Sci. 97, 1355–1358.
Porter, S.C., An, Z., 1995. Correlation between climate events in the North Atlantic and China during the last glaciation. Nature 375, 305–308.
Qian, X.P., 1960. Development of the carbonate Karst, in Shanxi plateau. Hydrogeol. Eng. Geol. 4 (3), 19–23 (in Chinese).
Rao, Z.G., Chen, F.H., Cheng, H., Liu, W.G., Wang, G., Lai, Z.P., Bloemendal, J., 2013. High-resolution summer precipitation variations in the western Chinese Loess Plateau during the last glacial. Sci. Rep. 3, 2785.
Rasmussen, S.O., Bigler, M., Blockley, S.P., Blunier, T., Buchardt, S.L., Clausen, H.B., Cvijanovic, I., Dahl-Jensen, D., Johnsen, S.J., Fischer, H., Gkinis, V., Guillevic, M., Hoek, W.Z., Lowe, J.J., Pedro, J.B., Popp, T., Seierstad, I.K., Steffensen, J.P., Svensson, A.M., Vallelonga, P., Vinther, B.M., Walker, M.J.C., Wheatley, J.J., Winstrup, M., 2014. A stratigraphic framework for abrupt climatic changes during the Last Glacial period based on three synchronized Greenland ice-core records: refining and extending the INTIMATE event stratigraphy. Quat. Sci. Rev. 106, 14–28.
Rohling, E.J., Mayewski, P.A., Challenor, P., 2003. On the timing and mechanism of millennial-scale climate variability during the last glacial cycle. Clim. Dynam. 20, 257–267.
Rohling, E.J., Liu, Q.S., Roberts, A.P., Stanford, J.D., Rasmussen, S.O., Langen, P.L., Siddall, M., 2009. Controls on the East Asian monsoon during the last glacial cycle, based on comparison between Hulu Cave and polar ice-core records. Quat. Sci. Rev. 28, 3291–3302.
Scholz, D., Hoffmann, D.L., 2011. StalAge-an algorithm designed for construction of speleothem age models. Quat. Geochronol. 6, 369–382.
Shen, C.-C., Lawrence Edwards, R., Cheng, H., Dorale, J.A., Thomas, R.B., Bradley Moran, S., Weinstein, S.E., Edmonds, H.N., 2002. Uranium and thorium isotopic and concentration measurements by magnetic sector inductively coupled plasma mass spectrometry. Chem. Geol. 185, 165–178.
Shen, C.-C., Cheng, H., Edwards, R.L., Moran, S.B., Edmonds, H.N., Hoff, J.A., Thomas, R.B., 2003. Measurement of attogram quantities of ^{231}Pa in dissolved and particulate fractions of seawater by isotope dilution thermal ionization mass spectroscopy. Anal. Chem. 75, 1075–1079.
Shen, C.-C., Kano, A., Hori, M., Lin, K., Chiu, T.C., Burr, G.S., 2010. East Asian monsoon evolution and reconciliation of climate records from Japan and Greenland during the last deglaciation. Quat. Sci. Rev. 29, 3327–3335.
Shen, C.C., Wu, C.C., Cheng, H., Edwards, R.L., Hsieh, Y.T., Gallet, S., Chang, C.-C., Li, T.Y., Lam, D.D., Kano, A., Hori, M., Spötl, C., 2012. High-precision and high-resolution carbonate ^{230}Th dating by MC-ICP-MS with SEM protocols. Geochim. Cosmochim. Acta 99, 71–86.
Skinner, L.C., 2008. Revisiting the absolute calibration of the Greenland ice-core age-scales. Clim. Past 4, 295–302.
Spötl, C., Mangini, A., Richards, D.A., 2006. Chronology and paleoenvironment of Marine Isotope Stage 3 from two high-elevation speleothems, Austrian Alps. Quat. Sci. Rev. 25, 1127–1136.
Stott, L., Poulsen, C., Lund, S., Thunell, R., 2002. Super ENSO and global climate oscillations at millennial time scales. Science 297, 222–226.
Svensson, A., Andersen, K.K., Bigler, M., Clausen, H.B., Dahl-Jensen, D., Davies, S.M., Johnsen, S.J., Muscheler, R., Parrenin, F., Rasmussen, S.O., Röthlisberger, R., Seierstad, I., Steffensen, J.P., Vinther, B.M., 2008. A 60000 year Greenland stratigraphic ice core chronology. Clim. Past 4, 47–57.
Voelker, A.H.L., 2002. Global distribution of centennial-scale records for Marine Isotope Stage (MIS) 3: a database. Quat. Sci. Rev. 21, 1185–1212.
Wang, H.J., Xue, F., 2003. Interannual variability of Somali jet and its influences on the inter-hemispheric water vapor transport and on the East Asian summer rainfall. Chin. J. Geophys. 1, 18–25 (in Chinese).
Wang, Y.J., Cheng, H., Edwards, R.L., An, Z.S., Wu, J.Y., Shen, C.-C., Dorale, J.A., 2001. A high-resolution absolute-dated Late Pleistocene monsoon record from Hulu Cave, China. Science 294, 2345–2348.
Wang, Y.J., Cheng, H., Edwards, R.L., Kong, X.G., Shao, X.H., Chen, S.T., Wu, J.Y., Jiang, X.Y., Wang, X.F., An, Z.S., 2008. Millennial- and orbital-scale changes in the East Asian monsoon over the past 224,000 years. Nature 451, 1090–1093.
Xue, F., Wang, H., He, J., 2004. Interannual variability of Mascarene high and Australian high and their influences on East Asian summer monsoon. J. Meteorol. Soc. Jpn. 82, 1173–1186.
Yuan, D., Cheng, H., Edwards, R.L., Dykoski, C.A., Kelly, M.J., Zhang, M., Qing, J., Lin, Y., Wang, Y., Wu, J., Dorale, J.A., An, Z., Cai, Y., 2004. Timing, duration, and transitions of the last interglacial Asian monsoon. Science 304, 575–578.
Zhao, K., Wang, Y.J., Edwards, R.L., Cheng, H., Liu, D.B., 2010. High-resolution stalagmite $\delta^{18}O$ records of Asian monsoon changes in central and southern China spanning the MIS 3/2 transition. Earth Planet Sci. Lett. 298 (1), 191–198.
Zhou, H.-Y., Zhao, J.-X., Feng, Y.-X., Chen, Q., Mi, X.-J., Shen, C.-C., He, H.B., Yang, L., Liu, S.-H., Chen, L., Huang, J.Y., Zhu, L.Y., 2014. Heinrich event 4 and Dansgaard/Oeschger events 5-10 recorded by high-resolution speleothem oxygen isotope data from central China. Quat. Res. 82, 394–404.